Journal of Power Sources 268 (2014) 733–743

Contents lists available at ScienceDirect

Journal of Power Sources

journal homepage: www.elsevier.com/locate/jpowsour

Influence of membrane properties on the transient behavior of polymer electrolyte fuel cells

A. Verma, R. Pitchumani*

Advanced Materials and Technologies Laboratory, Department of Mechanical Engineering, Virginia Tech, Blacksburg, VA 24061-0238, USA

HIGHLIGHTS

- Presents a detailed computational modeling of dynamic performance of PEM fuel cells.
- Analyzes the effects of membrane properties on the fuel cell performance and water management.
- Presents a novel graded design of membrane to prevent voltage reversals and dryout.

ARTICLE INFO

Article history:
Received 23 December 2013
Received in revised form
11 June 2014
Accepted 11 June 2014
Available online 18 June 2014

Keywords:
Polymer electrolyte membrane fuel cell
Computational modeling
Membrane hydration
Transient response
Graded membrane design
Membrane dryout

ABSTRACT

Understanding the performance of proton exchange membrane (PEM) fuel cells is critical to the water management in the fuel cell system. Low-humidity operating conditions present a complex interaction between dynamic behavior and water transport owing to different time scales of water transport mechanisms in the transient process. Toward understanding the effects of membrane properties on the dynamic behavior, this paper presents numerical simulations for a single channel PEM fuel cell undergoing changes in load, by subjecting the unit cell to step change in current. The complex interaction between cell voltage response and water transport dynamics for various membrane properties is explored in detail, where the performance is critically related to the water content of the membrane. Detailed computational fluid dynamics (CFD) simulations are carried out to show that step increase in current density leads to anode dryout due to electro-osmotic drag, and to investigate the dependence of transient behavior on the variations in membrane properties. The results show that water uptake by the membrane is a crucial factor in determining the occurrence of anode dryout and hence voltage reversal, and can be avoided by a graded membrane design.

1. Introduction

Proton exchange membrane (PEM) fuel cells offer much potential as energy efficient, clean and quiet, energy conversion devices for mobile and stationary applications. Due to major improvements in catalyst loading and membrane technology, PEM fuel cells have seen increased usage in various applications. A further reduction in cost can be achieved through better design and improved performance and durability of the fuel cells. This objective has generated much interest for research in control and optimization of transport and electrochemical processes in fuel cells [1,2]. While most of the research has been focused on steady-state operation, use of PEM fuel cells for automotive applications, where there are rapid changes in load, presents a need for better understanding of their transient behavior.

A PEM fuel cell is composed of membrane electrode assembly (MEA), sandwiched between porous gas diffusion layers (GDL) on either side, and bipolar plates with grooved-in gas channels of serpentine or interdigitated configurations. Humidified hydrogen (H_2) and oxygen (O_2) or air are transported, through anode and cathode flow channels, respectively, and are flowed through diffusion layers to react at the catalyst layers of the MEA. Hydrogen dissociates at the anode catalyst to produce protons that are transported across the thickness of the membrane to the cathode catalyst later where it combines with oxygen and electrons, flowing through an external circuit from the anode catalyst layer to the cathode catalyst layer, to produce water.

The performance of a fuel cell is critically related to the membrane hydration, as it affects the proton conductivity through membrane—a higher water content (number of water molecules per sulfonic acid group) in the membrane ensures higher

* Corresponding author. Tel.: +1 540 231 1776.
E-mail address: pitchu@vt.edu (R. Pitchumani).

http://dx.doi.org/10.1016/j.jpowsour.2014.06.065
0378-7753/

conductivity. Under low-humidity operation, suitable for automotive applications, electro-osmotic drag, back-water diffusion and rate of water supply or removal through humidified reactants, each associated with different time scales, interact in complex ways to affect the transient behavior of PEM fuel cells. The step increase in current density causes the anode side of the membrane to quickly dryout owing to electro-osmotic drag whereas back-diffusion of water from cathode to anode takes longer to rehydrate the membrane. This can lead to temporary dryout and hence sharp voltage drop, owing to jump in membrane resistance. As the back-diffusion rehydrates the anode side, the voltage recovers, improving the performance. The above transient behavior is strongly dependent on the transport and physical properties of the membrane namely, the water diffusion coefficient, electro-osmotic drag coefficient, thickness and equivalent weight, and needs to be studied in detail. Understanding the transient behavior and effect of membrane properties is of paramount importance for PEM fuel cells to be successfully deployed for mobile applications [1,2].

Several researchers have attempted to study the transient behavior of PEM fuel cells experimentally and numerically [3–14]. Hamelin et al. [3] studied the behavior and performance of a proton exchange membrane fuel cell stack for fast load commutations, observing that the system response was faster than 0.15 s. Kim et al. [4,5] investigated the effects of stoichiometry, reservoir and fuel dilution on the transient response of fuel cell, and elucidated the undershoot and overshoot characteristics for change in loads at fixed flow rate. Benziger et al. [6] studied the dynamic response of a stirred tank reactor (STR) PEM fuel cell for changes in load, emphasizing the role of membrane water uptake in ignition and extinguished state of the fuel cell. Yan et al. [7], in their experiments, investigated the steady state and dynamic performance of PEM fuel cells. The results showed cathode humidity, stoichiometric flow ratio and cell temperature as key parameters affecting the performance and being related to the water transport. The above studies point the importance of water transport and membrane hydration in the performance and transient response of fuel cells.

The transient response of fuel cells has been investigated numerically in several studies. The model by Um et al. [8] assumed constant water content and investigated the transient response of fuel cell, emphasizing the effects of reactant diffusion. Amphlett et al. [9] developed a lumped-parameter based thermal model to predict the transient response, while using steady-state electrochemical kinetics. Pathapati et al. [10] and Xue et al. [11] developed simplified system level models for their transient study. Ceraolo [12] used a simplified one-dimensional model to study the dynamic behavior, considering only the cathode side. These numerical studies used simplified models and lacked detail representation of complex interactions during transient operations. A more complete model was developed by Wang and Wang [13,14], extending the model used in Ref. [8] to include the effects of water accumulation and electrochemical double layer discharge. The transient model explored the dynamic behavior for step change in humidity, voltage and current, emphasizing the different time scales characteristic to transport and electrochemical process. To the authors' knowledge, Wang and Wang [14] were the first to simulate the effects of step changes in current load. The effects of two different membrane thicknesses on the dynamic behavior were studied in detail. It was pointed out in their study that the increase in current density leads to drying of anode leading to sudden drop in voltage.

In the present study, computational fluid dynamics (CFD) simulations are carried out using the model developed in Ref. [14] to study the effect of step change in current density. Although the work by Wang and Wang [14] provides mathematically rigorous description of the governing physics, the transport properties vary extensively by orders of magnitude and their influence has not been addressed in detail in previous studies. Majsztrik [15] presented an elaborate compilation of the diffusivity values of water in Nafion and the experimental techniques used, with values spanning over three orders of magnitude, at a single temperature. Similarly, the variations in water uptake, electro-osmotic drag coefficient, ionic-conductivity of membrane have been presented in Refs. [16–18], respectively. The variations in the physical and transport properties of GDL and membrane play an important role in determining the transient behavior of membrane and are addressed in detail in the present study. The mathematical model used as the basis of the study is presented in Section 2 and the results are reported and discussed in Section 3.

2. Mathematical model

Fig. 1 shows a schematic view of the two-dimensional (2D) section of a single channel PEM fuel cell corresponding to the geometry of the model considered in this study. Bipolar plates, gas channels, gas diffusion layers and catalyst layers on anode and cathode sides of a membrane constitute the different regions for this study. A two-dimensional, single phase, transient, isothermal model, following the assumptions in Refs. [1,13,14], is used to simulate the fuel cell dynamics with the objective of accurately capturing the transient water content distribution in the membrane. Owing to the low Reynolds number of the flow in gas channels laminar flow is assumed. The model takes into consideration important transient processes such as gas transport, water accumulation, and electrochemical double layer discharge. A single-channel of the fuel cell forms the computational domain for this study. The equations governing the dynamics of fuel cell behavior are as follows [13,14,19]:

$$\text{Continuity}: \ \nabla\cdot\vec{u} = 0 \tag{1}$$

$$\text{Momentum}: \ \frac{1}{\varepsilon}\left[\frac{\partial\vec{u}}{\partial t} + \frac{1}{\varepsilon}\nabla\cdot(\vec{u}\,\vec{u})\right] = -\nabla\cdot\left(\frac{p}{\rho}\right) + \nabla\cdot\tau + S_u \tag{2}$$

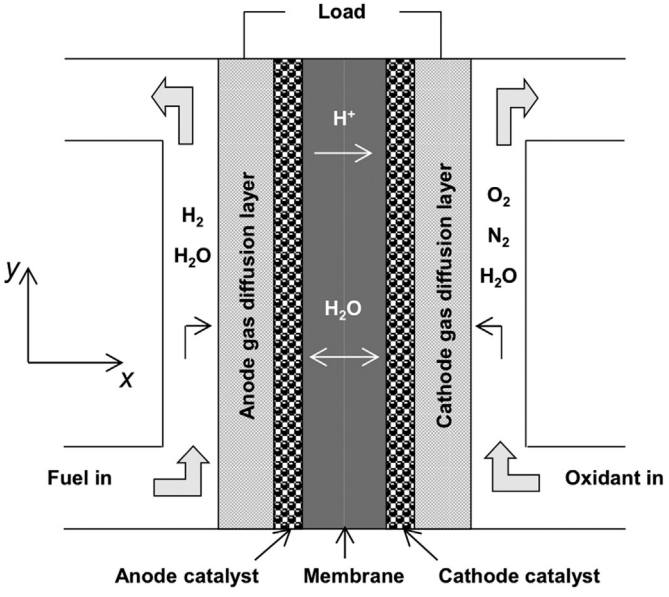

Fig. 1. Schematic view of the two-dimensional (2D) section of a single channel PEM fuel cell.

$$\text{Species}: \ \varepsilon\frac{\partial C_k}{\partial t}+\nabla\cdot(\vec{u}C_k)=\nabla\cdot\left(D_k^{\text{eff}}\nabla C_k\right)+S_k \tag{3}$$

$$\text{Charge Transport}: \ \nabla\cdot\left(\sigma_k^{\text{eff}}\nabla\phi_i\right)+S_i=0; \quad i=s,\ m \tag{4}$$

where $\vec{u}$ is the superficial velocity vector or volume averaged velocity, ε is the porosity of the porous media and equals unity in gas channels, p is the pressure, τ is the stress tensor, ρ represents the density, C_k denotes the molar concentration of species k namely, H_2, O_2 and H_2O, and the effective diffusivity D_k^{eff} is expressed as [20]:

$$D_k^{\text{eff}}=\varepsilon_{\text{eff}}^{1.5}D_k \tag{5}$$

where D_k is the diffusivity of each species and can be expressed as a function of temperature T and pressure p as:

$$D_k=D_{k,\text{ref}}\left(\frac{T}{353}\right)^{1.5}\left(\frac{1}{p}\right) \tag{6}$$

Eq. (3) is used to describe water transport in MEA by expressing ε as [13,14]:

$$\varepsilon=\varepsilon_g+\varepsilon_m\frac{dC_w^m}{dC_w}=\varepsilon_g+\varepsilon_m\frac{\rho_m}{\text{EW}}\frac{RT}{p^{\text{sat}}}\frac{d\lambda}{da} \tag{7}$$

where ρ_m is the density of the dry membrane, subscripts g and m, respectively, represent gas and membrane phase, R is the universal gas constant, and EW is the equivalent weight of the dry membrane, taken to be 1.1 kg mol^{-1}. The membrane water content, λ, can be calculated from Ref. [21]:

$$\lambda=\begin{cases}0.043+17.81a-39.85a^2+36.0a^3 & 0\le a\le 1\\ 14+1.4(a-1) & 1\le a\le 3\\ 16.8 & 3<a\end{cases} \tag{8}$$

in which, the water activity a is expressed as:

$$a=\frac{C_wRT}{p^{\text{sat}}} \tag{9}$$

and the saturation pressure for water, p^{sat}, is given by:

$$\begin{aligned}\log_{10}p^{\text{sat}}=&-2.1794+0.022953(T-273.15)-9.1837\\&\times10^{-5}(T-273.15)^2+1.4454\\&\times10^{-7}(T-273.15)^3\end{aligned} \tag{10}$$

The diffusivity of water in membrane is determined using the following relationship [22]:

$$D_w^m=\begin{cases}3.1\times10^{-5}\lambda\left(e^{0.28\lambda}-1\right)e^{-\frac{2346}{T}} & 0\le\lambda\le3\\ 4.17\times10^{-8}\lambda\left(1+161e^{-\lambda}\right)e^{-\frac{2346}{T}} & \lambda>3\end{cases} \tag{11}$$

A constant density is assumed with no mass source terms, following the assumptions in Refs. [8,9]; The source term, S_u in Eq. (2), incorporates the effect of porous media on flow and is expressed in Table 1; The subscripts s and m in Eq. (4) represent the solid and membrane phases, respectively, ϕ_i is the i-phase potential, σ_i^{eff} represents effective charge conductivity for the i-th phase, and the source term S_i is a function of the transfer current density (j) in the catalyst layers and is expressed in Table 1. The ionic conductivity of the membrane σ_m is given by Ref. [16]:

Table 1
Source terms in the governing equations.

Domain	S_u	S_k	S_s, S_m
Gas channels	0	0	0
Diffusion layers	$-(\mu/K_{\text{GDL}})\vec{u}$	0	0
Catalyst layers	$-(\mu/K_{\text{GDL}})\vec{u}$	Anode: $-j_a/2F$ $(i=H_2)$ 0 $(i=O_2)$ $-\nabla\cdot(n_di_e/F)$ $(i=H_2O)$ Cathode: 0 $(i=H_2)$ $-j_c/4F$ $(i=O_2)$ $j_c/2F-\nabla\cdot(n_di_e/F)$ $(i=H_2O)$	Anode: $S_s=-j_a<0$ $S_m=+j_a<0$ Cathode: $S_s=+j_c>0$ $S_m=-j_c<0$
Membrane	$-(\mu/K_{\text{GDL}})\vec{u}$	0	0

$$\sigma_m=(0.005139\lambda-0.00326)\exp\left[1286\left(\frac{1}{303}-\frac{1}{T}\right)\right] \tag{12}$$

The current generation in the catalyst layers is governed by the Butler–Volmer equation, which can be expressed in a simplified form as

$$j_a=j_a^{\text{ref}}\left(\frac{C_{H_2}}{C_{H_2}^{\text{ref}}}\right)\left(\frac{\alpha_a+\alpha_c}{RT}F\eta\right) \tag{13}$$

$$j_c=j_c^{\text{ref}}\left(\frac{C_{O_2}}{C_{O_2}^{\text{ref}}}\right)\exp\left(\frac{\alpha_cF\eta}{RT}\right) \tag{14}$$

where subscripts a and c denote anode and cathode, respectively, j^{ref} is the reference volumetric exchange current density, α is the transfer coefficient, C_{H_2} and C_{O_2} are the molar concentrations of H_2 and O_2, respectively, F is the Faraday constant, and η is the surface over-potential, is given by:

$$\eta=\phi_s-\phi_m-V_{\text{ref}} \tag{15}$$

where V_{ref} is 0 at the anode and is equal to the open circuit voltage, V_{OCV}, at the cathode, given in terms of temperature T as:

$$V_{\text{OCV}}=1.23-0.9\times10^{-3}(T-298) \tag{16}$$

Eqs. (1)–(4) form a complete set of governing equations with nine unknowns: $\vec{u}$ (three components), p, C_{H_2}, C_{O_2}, C_{H_2O}, ϕ_s, ϕ_m. The governing equations are subject to appropriate boundary and interface conditions, shown in Fig. 2. At the flow inlet boundaries, $u_{H_2}^{\text{in}}=0.1771$ m s^{-1}, $u_{\text{Air}}^{\text{in}}=0.4765$ m s^{-1}, $\text{RH}_a^{\text{in}}=50\%$, and $\text{RH}_c^{\text{in}}=0\%$. The values correspond to the stoichiometric flow ratio of 1.5 at anode and 2.0 at cathode, with the relative humidity values depicting the low-humidity PEMFC operation [14].

The governing Eqs. (1)–(4), with above the boundary conditions are solved using a control volume based commercial fluid dynamics (CFD) package, ANSYS/Fluent® [25] using the pressure-implicit with splitting of operators (PISO) algorithm. The specific governing equations and the corresponding source terms are implemented through user-defined functions and user-defined scalars (species and phase potentials). A systematic mesh size convergence check was conducted such that the difference in the results was less than 0.5% for further reduction in mesh size. About 3500 computational cells are used to capture the detailed electrochemical and physical phenomenon. In order to accurately capture the anode dryout and thus voltage reversal, a maximum time step of 0.1 s was found to be optimal for the simulations. A constant time step of 0.1 s is used for the simulations; with a run time of approximately 6 h on an Intel® Xeon™ Processor 3.33 GHz. A load change is imposed at

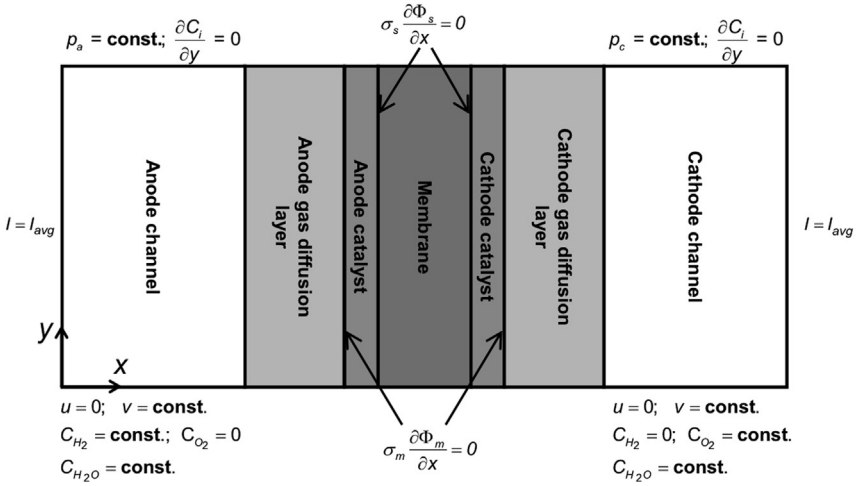

Fig. 2. Schematic illustration of the boundary and interface conditions used in the modeling.

the initial time, $t = 0$, by specifying the change in the current density, I, as a boundary condition. The geometrical, physical and electrochemical parameters used in this study are listed in Table 2.

3. Results and discussion

The numerical model described in the previous section is first validated by comparing the cell voltage (E_{cell}) response with the numerical results reported by Wang and Wang [14]. Fig. 3 shows the cell voltage variation with current density for step change in current density from $I = 0.1$ to 0.4, 0.5, 0.6, 0.7 A cm^{-2}, where the solid lines represent the results from present simulations, and the results from Ref. [14] are indicated by dashed lines. It can be seen that the cell voltage drops instantaneously owing to the time-scale associated with the electrochemical double layer discharge, on the order of micro-to-milli-seconds. In addition, at low-humidity operating conditions, the voltage response is seen in Fig. 3 to exhibit an undershoot, with the degree of undershoot increasing as the magnitude of current change is increased. For $I = 0.7$ A cm^{-2}, Fig. 3 shows that the voltage drops to zero, indicating a voltage reversal. The undershoot in the voltage response can be attributed to the jump in water electro-osmotic drag, which increases proportionally to the step change in the current density. This causes the anode to dryout and, in turn, increases the membrane resistance, leading to further drop in the voltage to a minimum. As the membrane at anode is rehydrated, the membrane resistance decreases, leading to increase in voltage and achieving steady state. The time scale associated with the back-diffusion of water dictates the time taken for the voltage response to improve, and is on the order of 0.7 s for the parametric combination considered. The figure shows close agreement between the voltage response obtained for the present simulations and those reported in Ref. [14].

The comparisons presented in Fig. 3 demonstrate the capabilities of the present model to accurately capture the water transport dynamics and predict voltage response, which forms the basis of the further studies reported in this section. The effects of water diffusivity in the GDL, gas channels and the membrane, the equivalent weight of membrane, the electro-osmotic drag coefficient and water uptake in the membrane on the dynamic response of the fuel cell is presented in the following discussion. Temporal variations in cell voltage for step change in current load are plotted to elucidate the response and is discussed in detail.

Fig. 4(a)–(d) presents the transient variation in cell potential for various H_2O diffusivity values in the gas channel, $D^{ref}_{H_2O}$, as the current density is stepped up from (a) 0.1 A cm^{-2} to 0.4 A cm^{-2}, (b) 0.1 A cm^{-2} to 0.5 A cm^{-2}, (c) 0.1 A cm^{-2} to 0.6 A cm^{-2}, and (d) 0.1 A cm^{-2} to 0.7 A cm^{-2}, respectively. In each plot, the effect of water diffusivity in gas is investigated for diffusivity values ranging from 3.89×10^{-6} m^2 s^{-1} to 3.89×10^{-4} m^2 s^{-1}, while the diffusivity values of the other reactants are kept constant as specified in

Table 2
Geometrical and physical parameters used in the numerical simulations [8,9,14].

Parameter [units]	Symbol	Value
Gas channel depth [mm]		1.0
Diffusion layer thickness [mm]		0.3
Catalyst layer thickness [mm]		0.01
Membrane (N112) thickness [mm]		0.051
Fuel cell/gas channel length [mm]		100.0
Temperature [K]	T	353
Permeability of diffusion layer [m^2]	K_{GDL}	10^{-12}
Permeability of catalyst layer [m^2]	K_{CL}	10^{-15}
Gas diffusion layer porosity	ε_{GDL}	0.6
Catalyst layer porosity	ε_{CL}	0.4
Volume fraction membrane in catalyst layer	ε_m	0.26
Anode reference exchange current density [A m^{-3}]	$j_{a,ref}$	5.00×10^8
Cathode reference exchange current density [A m^{-3}]	$j_{c,ref}$	500
H_2 diffusivity membrane [m^2 s^{-1}]	$D_{H_2,mem}$	2.59×10^{-10}
H_2 diffusivity in gas [m^2 s^{-1}]	$D_{H_2,ref}$	1.1×10^{-4}
O_2 diffusivity in membrane [m^2 s^{-1}]	$D_{O_2,mem}$	1.22×10^{-10}
O_2 diffusivity in gas [m^2 s^{-1}]	$D_{O_2,ref}$	3.2348×10^{-5}
H_2O diffusivity in gas [m^2 s^{-1}]	$D_{H_2O,ref}$	7.35×10^{-5}

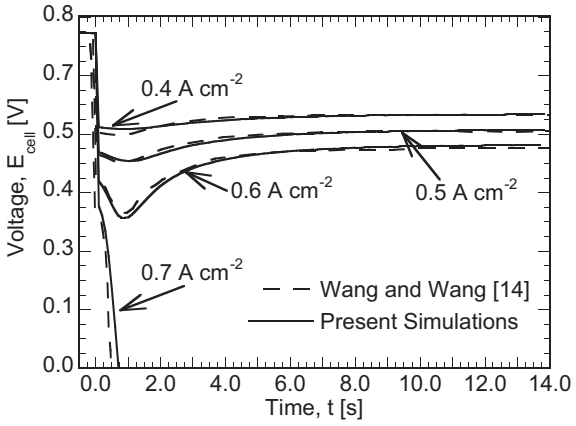

Fig. 3. Cell voltage variation with current density for step change in current density from $I = 0.1$ to 0.4, 0.5, 0.6, 0.7 A cm^{-2}.

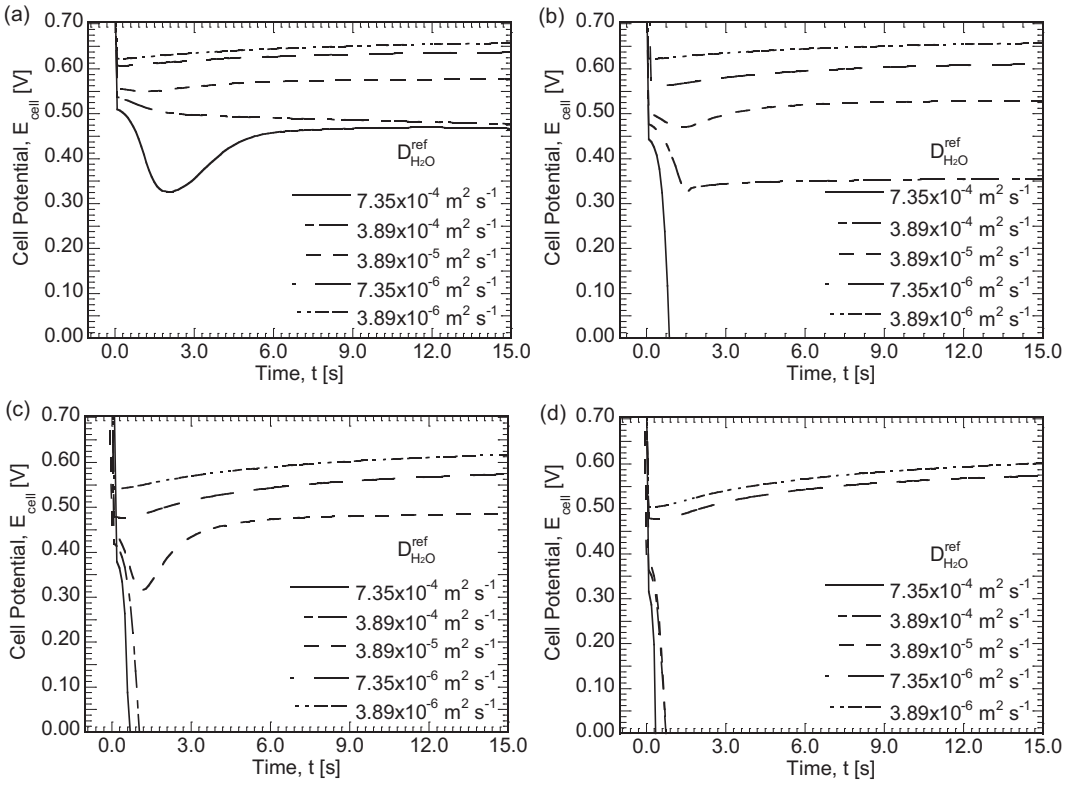

Fig. 4. Transient variation in cell potential for various $D^{ref}_{H_2O}$, for (a) 0.1 A cm^{-2} to 0.4 A cm^{-2}, (b) 0.1 A cm^{-2} to 0.5 A cm^{-2}, (c) 0.1 A cm^{-2} to 0.6 A cm^{-2}, and (d) 0.1 A cm^{-2} to 0.7 A cm^{-2}, respectively.

Table 1. From Fig. 4(a) it is observed that, following the instantaneous drop in cell voltage, which is attributed to the time scale associated with electrochemical double layer discharge as explained before, the cell voltage recovers to a steady state, for all the diffusivity values except for $D^{ref}_{H_2O} = 3.89 \times 10^{-4}$ m^2 s^{-1}. For $D^{ref}_{H_2O} = 7.35 \times 10^{-6}$ m^2 s^{-1}, the degree of voltage undershoot is the most, with voltage reaching a minimum at $t = 2$ s, as seen in Fig. 4(a). In contrast to that observed in Fig. 4(a), for a step change in current density from 0.1 A cm^{-2} to 0.5 A cm^{-2} (Fig. 4(b)), voltage reversal occurs for $D^{ref}_{H_2O} = 7.35 \times 10^{-4}$ m^2 s^{-1}, whereas for step change from 0.1 A cm^{-2} to 0.6 A cm^{-2} (Fig. 4(c)) voltage reversal occurs for $D^{ref}_{H_2O} = 3.89 \times 10^{-4}$ and 7.35×10^{-4} m^2 s^{-1} and for $D^{ref}_{H_2O} = 3.89 \times 10^{-4}$, 7.35×10^{-4} and 3.89×10^{-5} m^2 s^{-1} given step change in current density from 0.1 A cm^{-2} to 0.7 A cm^{-2} (Fig. 4(d)), resulting from anode dryout. Significant voltage undershoot is observed for $D^{ref}_{H_2O} = 7.35 \times 10^{-4}$ m^2 s^{-1} in Fig. 4(a) which is recovered with back-diffusion of water to the anode, with an undershoot of around 0.2 V. It can be seen in Fig. 4(a)–(d) that there exists a non-monotonic trend associated with variation in steady state cell potential values for different diffusivity values, with $D^{ref}_{H_2O} = 7.35 \times 10^{-4}$ m^2 s^{-1} and 3.89×10^{-6} m^2 s^{-1} defining the minimum and maximum values of steady state voltages, respectively, in Fig. 4(a). The diffusivity at the porous layers determines the rate at water is transported to and from the anode and the cathode sides, determining the amount of water contained in the membrane. It is also noted that, for lower diffusivity values, voltage reversals are not observed (Fig. 4(a)–(d)). Although the properties of membrane are fixed, change in diffusivity values of water in porous layers presents a complex dynamic behavior affecting the time scales for voltage recovery. Therefore, it can be established that water diffusion through porous layers significantly affects the water distribution process, thus determining the voltage response for change in current.

Fig. 5(a)–(d) depicts the change in cell potential with time for different values of water diffusivity in the membrane as the current density undergoes a step change from (a) 0.1 A cm^{-2} to 0.4 A cm^{-2}, (b) 0.5 A cm^{-2}, (d) 0.6 A cm^{-2} and (d) 0.7 A cm^{-2}, respectively. The water diffusivity in membrane D^w_m is a function of the membrane water content, λ, and temperature, T, as defined in Eq. (11). The effect of variation in membrane diffusivity is studied by varying $D^{w^*}_m$, where $D^{w^*}_m$ is a dimensionless parameter defined by $D^{w^*}_m = D^w_m$/Eq. (11). In the present study, $D^{w^*}_m$ is varied from 0.2 to 5 for the cases described above, while the other properties are fixed as given in Table 1. The change in net diffusion of water through the membrane can be also attributed to the changes in temperature and membrane thickness, thus the corresponding effects are not evaluated independently but can be represented by variations in the effective water diffusivity in the membrane.

In Fig. 5(a) it can be seen that $D^{w^*}_m = 0.5$ almost defines the limiting case for voltage reversal. As seen from Fig. 5(a)–(c), the voltage reversal occurs for $D^{w^*}_m < 1.0$, whereas voltage reversal occurs for $D^{w^*}_m < 2.0$ for step change in current density from 0.1 to 0.7 A cm^{-2} (Fig. 5(d)). Owing to the higher magnitude of step changes in current density, from 0.1 to 0.6 A cm^{-2} and 0.1–0.7 A cm^{-2} in Fig. 5(c) and (d), respectively, voltage reversal occurs for a relatively high diffusivity value compared to that is observed in Fig. 5(a) and (b). Also, it is noted that for $D^{w^*}_m = 1.0$, the extent of undershoot observed in the voltage is much larger in Fig. 5(c) compared to those observed in Fig. 5(a) and (b). It can be seen from Fig. 5(d) that, for $D^{w^*}_m = 1.0$, the cell undergoes voltage reversal for step change in current density from 0.1 to 0.7 A cm^{-2}. Although, voltage reversal also occurs for $D^{w^*}_m = 0.5$, for a step change in current density from 0.1 A cm^{-2} to 0.4 A cm^{-2} (Fig. 5(a)), the cell voltage recovers upon rehydration, after a reversal period

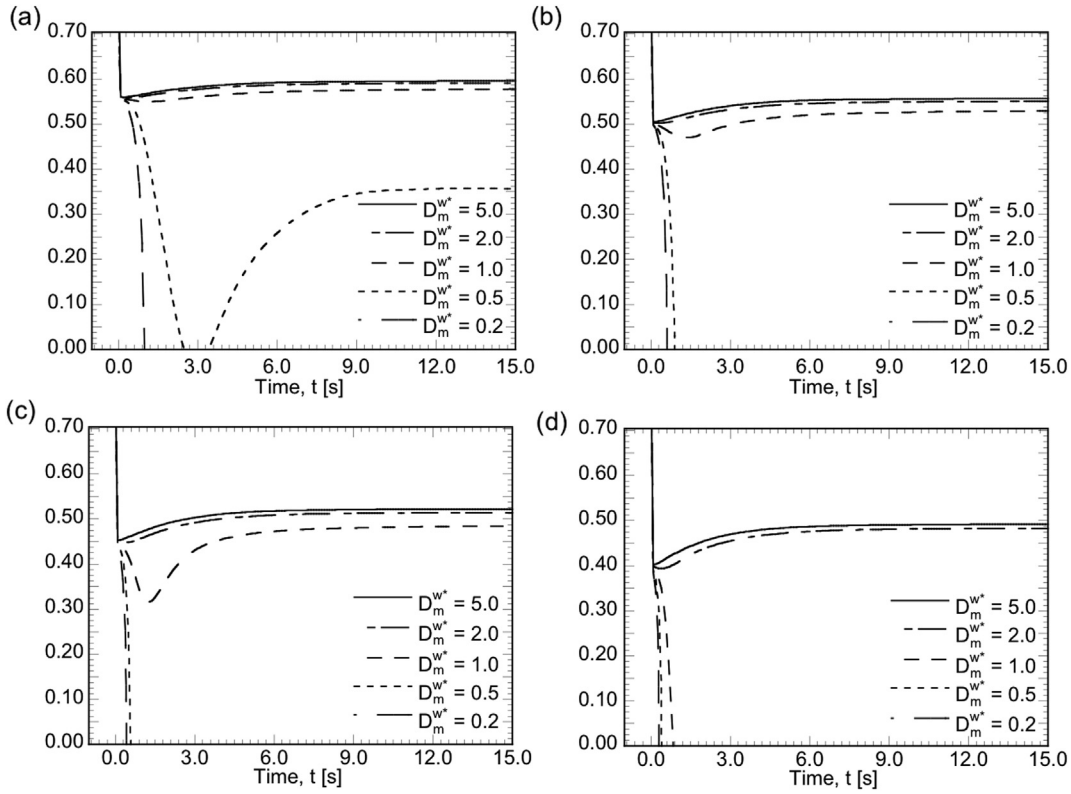

Fig. 5. Transient variation in cell potential for various D_m^w, for (a) 0.1 A cm^{-2} to 0.4 A cm^{-2}, (b) 0.1 A cm^{-2} to 0.5 A cm^{-2}, (c) 0.1 A cm^{-2} to 0.6 A cm^{-2}, and (d) 0.1 A cm^{-2} to 0.7 A cm^{-2}, respectively.

from $t = 2.5$–3.5 s. For the higher diffusivity values, no undershoot is observed and the cell reaches steady state following the expected initial instantaneous decrease in cell voltage, as illustrated in Fig. 5(a)–(d) for $D_m^{w^*} > 2$. This behavior can be attributed to the increased transport rate of water generated at cathode to anode through back-diffusion. The diffusivity of water through membrane effects the distribution of water in the membrane, both through the thickness and along the direction of flow, thus affecting the steady state cell potential values. In Fig. 5(a), it can be seen that steady state values are nearly unaffected for $D_m^{w^*} > 1.0$, whereas at $D_m^{w^*} = 0.5$, the steady state recovered voltage value is much lower. Similar behavior is observed for $D_m^{w^*} > 2.0$ in Fig. 5(b)–(d), with the difference in the steady state voltage recovery value increasing with increasing amplitude of change in current density.

These trends can also be used to qualitatively explain the effect of change in thickness of membrane on the transient response, where $D_m^{w^*} > 1.0$ would represent decrease in thickness of membrane and $D_m^{w^*} < 1.0$ would represent increase from the base value. The decrease in thickness leads to increase in rate at which water is transported back to anode through back-diffusion, thus affecting the dynamic response. The decrease in thickness causes the membrane to fail early due to reduced structural ability and thus use of reinforced membranes with better structural stability is desirable.

The equivalent molecular weight of dry membrane in kg mol^{-1} is denoted as EW, with lower values of EW indicating higher moles per kg, and, in turn, increased number of sulfonic acid groups. Increase in number of sulfonic acid groups leads to an increase in the amount of water stored in the unit mass membrane, for a given water activity. An increase in EW leads to a decrease in the amount of water that can be accumulated by membrane for a given water activity. The effect of variations in EW on the dynamic response is presented in Fig. 6. Fig. 6(a)–(d) depicts the cell voltage response for change in current density from (a) 0.1 A cm^{-2} to 0.4 A cm^{-2}, (b) 0.1 A cm^{-2} to 0.5 A cm^{-2}, (c) 0.1 A cm^{-2} to 0.6 A cm^{-2} and (d) 0.1 A cm^{-2} to 0.7 A cm^{-2}, respectively, for various equivalent weights, EW. The results presented in Figs. 4 and 5 were based on EW = 1.1 and Fig. 6 shows the effect of varying EW from 0.9 to 1.4, in steps of 0.1. Similar to the observations in Figs. 4 and 5, a step change in current density is seen in Fig. 6(a)–(d) to lead to sudden drop in voltage, followed by an undershoot due to membrane dryout and recovery on rehydration from back-diffusion of water to anode. It can be seen in Fig. 6(a) that an increase in EW from 0.9 to 1.4 leads to an increase in the degree of undershoot, with cell voltages approaching different steady state values for different EW's over time. For the change in current density from 0.1 to 0.5 A cm^{-2} (Fig. 6(b)), there is an increase in the amount of observed undershoot compared to that observed in Fig. 6(a), owing to increase in current density from 0.4 to 0.5 A cm^{-2}.

Similar behavior is observed in Fig. 6(c) and (d), with an exception of voltage reversal for EW > 1.2 in Fig. 6(c) and EW > 1.0 in Fig. 6(d). The increase in the degree of undershoot can be attributed to a faster dryout of anode side of the membrane, with increase in EW, as the same amount of water is dragged to the cathode but the holding capacity is reduced with increase in EW. As previously observed in Fig. 5, the steady state cell voltage values vary monotonically with EW. It is also noted from Fig. 6(a)–(d) that with increase in EW the time taken for the membrane to rehydrate also increases. The time taken by the cell potential to reach a steady state value is dependent on the time scale associated with time constant for membrane hydration, which is inversely proportional to EW.

Fig. 7(a)–(d) shows the temporal variation in cell potential for various electro-osmotic drag coefficient, n_d, values as the current

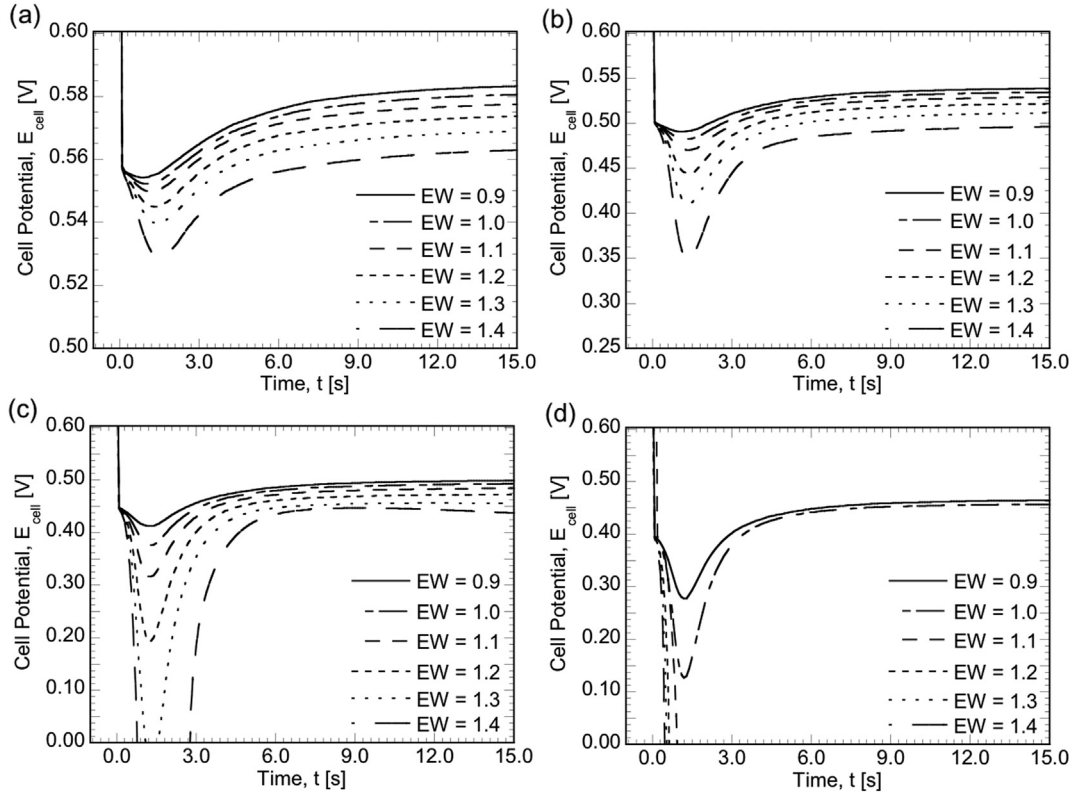

Fig. 6. Transient variation in cell potential for various EW, for (a) 0.1 A cm^{-2} to 0.4 A cm^{-2}, (b) 0.1 A cm^{-2} to 0.5 A cm^{-2}, (c) 0.1 A cm^{-2} to 0.6 A cm^{-2}, and (d) 0.1 A cm^{-2} to 0.7 A cm^{-2}, respectively.

density undergoes a step change from (a) 0.1 A cm^{-2} to 0.4 A cm^{-2}, (b) 0.1 A cm^{-2} to 0.5 A cm^{-2}, (c) 0.1 A cm^{-2} to 0.6 A cm^{-2} and (d) 0.1 A cm^{-2} to 0.7 A cm^{-2}, respectively. The electro-osmotic drag coefficient gives a representative figure of the effective moles of water transported per mole of protons conducted from anode to cathode catalyst layer and appears as a source term (Table 1) in species conservation equation for water Eq. (4). The values of n_d used in the present study range from 0.7 to 2.0, following the values reported in Refs. [15–18]. Note that larger values of n_d indicate more water being transported from anode to cathode, for a specified current density. It can be seen in Fig. 7(a) that cell voltage reaches zero for $n_d > 1.3$, whereas owing to increase in current density to 0.5 A cm^{-2} in Fig. 7(b), the voltage reaches zero and finally reverses for $n_d > 1.2$. Similar behavior is observed for $n_d > 1.1$ for step change in current density to 0.6 A cm^{-2} in Fig. 7(c) and for $n_d > 0.9$ for change to 0.7 A cm^{-2} in Fig. 7(d). It is also noted in Fig. 7(a) that there is no observable undershoot in voltage due to drag for $n_d < 1.0$, and the voltage recovers as the membrane is further hydrated by back-diffusion. Similar behavior is observed for $n_d < 0.9$ in Fig. 7(b) and for $n_d < 0.8$ in Fig. 7(c), whereas in Fig. 7(d) there exists an undershoot for the all the values of n_d studied. The steady state cell voltage values for 0.4 A cm^{-2} (Fig. 7(a)), 0.5 A cm^{-2} (Fig. 7(b)), 0.6 A cm^{-2} (Fig. 7(c)) and 0.7 A cm^{-2} (Fig. 7(d)) exhibit monotonic trend for variation in n_d. This behavior can be attributed to increased membrane resistance, due to lower membrane water content as the rate at which water is transported from anode to cathode increases. Also, it can be seen that degree of voltage undershoot is relatively smaller in Fig. 7(a) compared to that observed in Fig. 7(b)–(d) owing to smaller current density with minima of 0.49 V for $n_d = 1.3$ (Fig. 7(a)), whereas voltage reversal occurs for $n_d = 1.3$ in other cases.

Following the same format in Fig. 7, Fig. 8(a)–(d) depicts the change in cell potential over time for different values of water uptake in membrane as the current density is changed as a step from (a) 0.1 A cm^{-2} to 0.4 A cm^{-2}, (b) 0.1 A cm^{-2} to 0.5 A cm^{-2}, (c) 0.1 A cm^{-2} to 0.6 A cm^{-2} and (d) 0.1 A cm^{-2} to 0.7 A cm^{-2}, respectively. The water concentration in membrane, C_m^w, is a function of the membrane water content, λ, equivalent weight of membrane, EW, and density of the membrane, and is defined as $C_m^w = \rho\lambda/\mathrm{EW}$. The effect of variation in membrane water content is studied by varying $C_m^{w^*}$ in Fig. 8, where $C_m^{w^*}$ is a dimensionless parameter, given by $C_m^{w^*} = C_m^w/(\rho\lambda/\mathrm{EW})$. In the present study $C_m^{w^*}$ is varied from 0.8 to 1.2 for the cases described above. The above values are chosen to provide a systematic parametric study with a base of 1.0. The change in amount of water stored in the membrane can be achieved by changing the EW, λ, and density of membrane. The water content of the membrane, λ, is a function of water activity, a, which is function of temperature (Eq. (8)). At high temperature, for a given concentration of water in gas, the amount of water stored in the membrane is lower, thus increasing the temperature during operation leads to lowering of water content in membranes. It can be seen from Fig. 8(a) that the increase in water uptake capacity leads to decrease in the amount of undershoot observed with a maximum undershoot for $C_m^{w^*} = 0.7$. This can be attributed to increased amount of water to be removed by drag until back-diffusion rehydrates the membrane. Similar behavior is observed in Fig. 8(b)–(d), with more pronounced undershoots, owing to higher current density. As seen from Fig. 8(a) and (b), no voltage reversal occurs for the values of $C_m^{w^*}$ studied, whereas voltage reversal occurs for $C_m^{w^*} < 0.9$ and $C_m^{w^*} < 1.1$ for step changes in current density from 0.1 to 0.6 A cm^{-2} (Fig. 8(c)) and from 0.1 to 0.7 A cm^{-2} (Fig. 8(d)), respectively. In Fig. 8(a) it can be seen that $C_m^{w^*} = 0.5$ almost defines the limiting case for voltage reversal. Although, voltage reversal occurs for $C_m^{w^*} = 0.8$, for a step change in current density from 0.1 A cm^{-2} to 0.6 A cm^{-2} (Fig. 8(c)), the cell

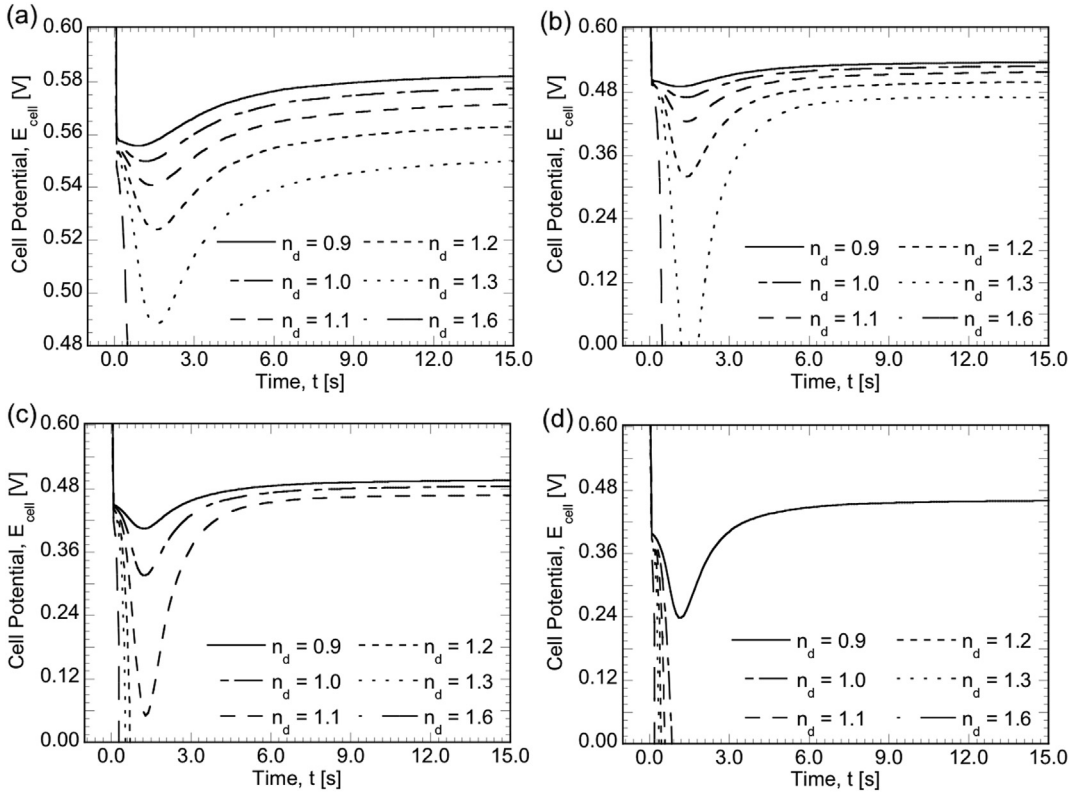

Fig. 7. Transient variation in cell potential for various n_d, for (a) 0.1 A cm^{-2} to 0.4 A cm^{-2}, (b) 0.1 A cm^{-2} to 0.5 A cm^{-2}, (c) 0.1 A cm^{-2} to 0.6 A cm^{-2}, and (d) 0.1 A cm^{-2} to 0.7 A cm^{-2}, respectively.

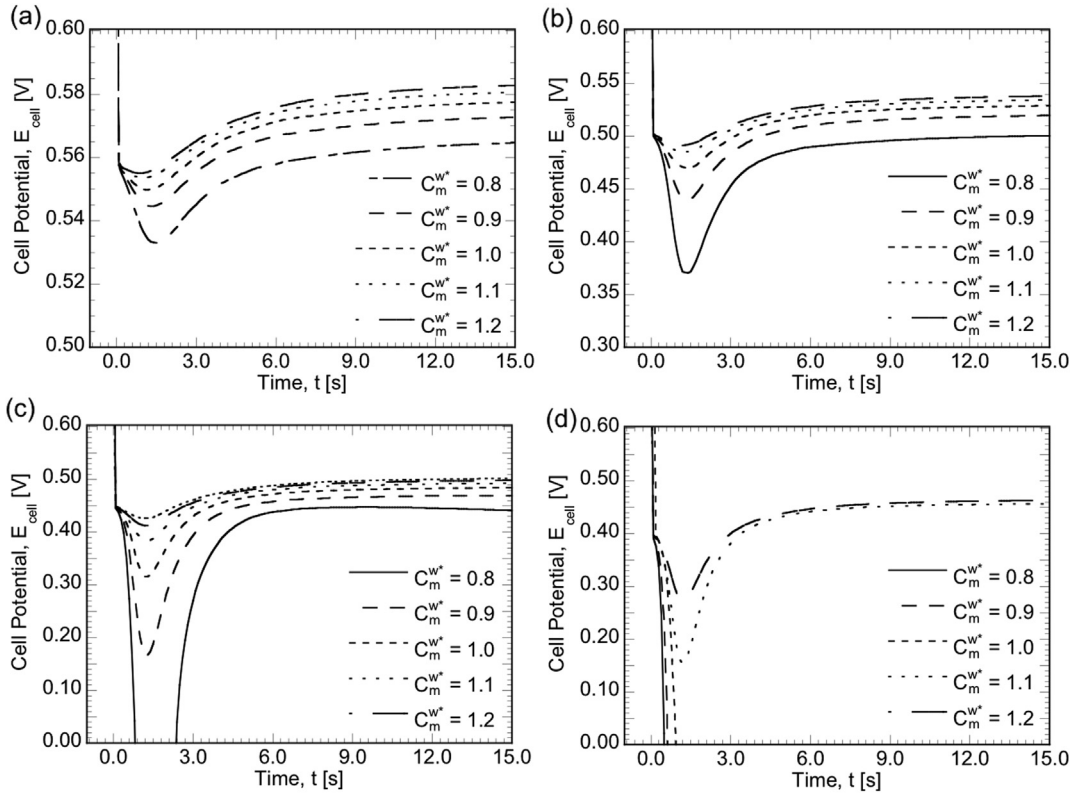

Fig. 8. Transient variation in cell potential for various C_m^w, for (a) 0.1 A cm^{-2} to 0.4 A cm^{-2}, (b) 0.1 A cm^{-2} to 0.5 A cm^{-2}, (c) 0.1 A cm^{-2} to 0.6 A cm^{-2}, and (d) 0.1 A cm^{-2} to 0.7 A cm^{-2}, respectively.

voltage recovers upon rehydration, after a reversal period from $t = 0.9–2.4$ s. For higher water uptake values the observed undershoot is low and the cell reaches steady state following the expected initial instantaneous decrease in cell voltage, as illustrated in Fig. 8(a)–(d), with steady state cell voltage increasing monotonically with increase in water uptake. This behavior can be attributed to the improved conductivity of protons from anode to cathode.

Similar to the format in Figs. 7 and 8, Fig. 9(a) and (b) depicts the change in cell potential over time for different values of ionic conductivity of protons in membrane as the current density is changed as a step from (a) 0.1 A cm^{-2} to 0.4 A cm^{-2} and (d) 0.1 A cm^{-2} to 0.6 A cm^{-2}, respectively. The ionic conductivity of membrane, σ_m, is a function of the membrane water content, λ, and operating temperature, T, and is defined as $\sigma_m = (0.005139\lambda - 0.00326)\exp[1286(1/303 - 1/T)]$. The effect of variation in ionic conductivity of the membrane is studied by varying σ_m^* in Fig. 9, where σ_m^* is a dimensionless parameter, given by $\sigma_m^* = \sigma_m/(0.005139\lambda - 0.00326)\exp[1286(1/303 - 1/T)]$. It can be seen from Fig. 9(a) that the steady state voltage increases with the increase in σ_m^*. It is also noted that for $\sigma_m^* = 0.25$ there is a significant drop in voltage upon step change in current density with the voltage almost reaching 0 before the anode region is replenished due to back diffusion. In contrast to the observation in Fig. 9(a) for step change in current density from 0.1 to 0.6 A cm^{-2} (Fig. 9(b)) the voltage reaches a value of 0 for $\sigma_m^* = 0.25$ and 0.50 owing to the dryout of the anode region. Similar to the observation in Fig. 9(a) it can be seen from Fig. 9(b) that the steady state voltage increases with the increase in σ_m^*.

It can be seen From Figs. 4 to 9 that the changes in diffusivity of water in the membrane, the electro-osmotic drag coefficient and ionic conductivity of the membrane, all lead to significant changes in transient behavior for step change in current density. It is noted

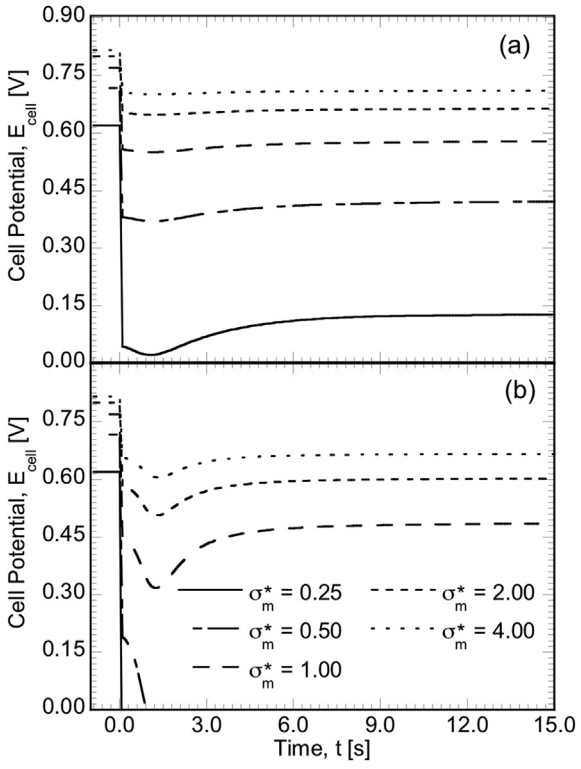

Fig. 9. Transient variation in cell potential for various σ_m, for (a) 0.1 A cm^{-2} to 0.4 A cm^{-2} and (b) 0.1 A cm^{-2} to 0.6 A cm^{-2}, respectively.

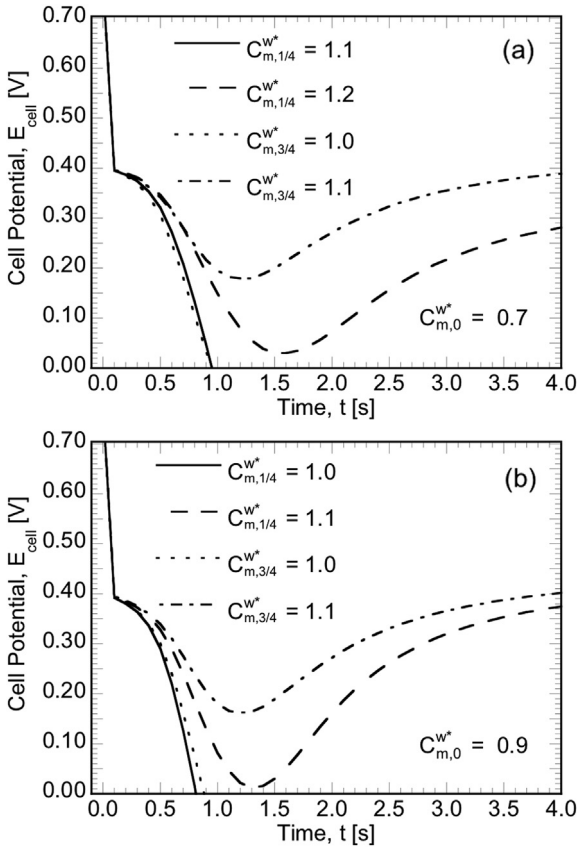

Fig. 10. Transient variation in cell potential for graded design of membrane for (a) $C^{w^*}_{m,b} = 0.7$, and (b) $C^{w^*}_{m,b} = 0.9$, respectively.

that the voltage reaches zero for $n_d > 1.3$, $D_m^{w^*} < 1.0$ and approaches zero for ionic conductivity, $\sigma_m < 0.50$, whereas for other properties the transient variation in voltage is not as significant given the similar variations in values of the membrane property. It can be inferred from the discussion in Fig. 8 that increasing the water content of the membrane improves its dynamic behavior, in particular, with regard to the voltage reversal. It is noted that the anode region dries out rapidly owing to electro-osmotic drag, leading to increase in proton transport resistance, followed by rehydration through back-diffusion. This suggests that an improvement in the water storage capacity of the membrane near the anode would lead to an improved dynamic behavior, by avoiding complete dryout. One possible approach is a membrane design with graded water content, instead of constant water content, decreasing across its thickness from the anode to the cathode, which could prevent anode dryout, thus avoiding voltage reversal and possible damage to membrane. To explore this concept, the water uptake in the membrane is altered in the region of the membrane near the anode while keeping the water uptake capacity of rest of the membrane to a fixed value. The graded water uptake is denoted with $C^{w^*}_{m,1/4}$, $C^{w^*}_{m,1/2}$, $C^{w^*}_{m,3/4}$ defining the water uptake capacity for 1/4th, 1/2 and 3/4th of the membrane thickness near the anode and $C^{w^*}_{m,0}$ defining the water uptake capacity for the rest of the membrane. The changes in water content values affect the transport properties of the membrane and were accounted for in the simulations accordingly.

Fig. 10(a) and (b) shows the effect of change in water uptake capacity in the parts of membrane on the dynamic behavior, for $C^{w^*}_{m,0} = 0.7$ and 0.9, respectively, given step change in current density form 0.1–0.7 A cm^{-2}. In each subplot, two different values

of each of $C^{w^*}_{m,1/4}$ and $C^{w^*}_{m,3/4}$ are shown by the different lines. Although not shown in Fig. 10, changing the water uptake capacity at the anode catalyst layer alone, with $C^{w^*}_m$ for rest of the membrane fixed to the $C^{w^*}_{m,0}$ could not avoid voltage reversal, for the values of $C^{w^*}_m$ studied. It can be seen from Fig. 10(a) that, for $C^{w^*}_{m,1/4} \leq 1.1$ the step change in current density leads to voltage reversal owing to the anode dryout, whereas a further increase in uptake capacity, for $C^{w^*}_{m,1/4} \geq 1.2$, the effects of back diffusion are dominant, avoiding voltage reversal. In comparison to that observed for $C^{w^*}_{m,1/4}$ in Fig. 10(a), for $C^{w^*}_{m,3/4}$ it can be seen that the cell voltage drops to zero for $C^{w^*}_{m,3/4} \leq 1.0$ and can be avoided for $C^{w^*}_{m,1/2} \geq 1.1$. For $C^{w^*}_{m,0} = 0.9$, Fig. 10(b) shows that in contrast to the observation for $C^{w^*}_{m,0} = 0.7$ (Fig. 10(a)), there exists no voltage reversals for $C^{w^*}_{m,1/4} \geq 1.1$. This behavior can be attributed to the increase in back diffusion rate owing to the increase in base water uptake capacity, $C^{w^*}_{m,0}$. Similar to the observation for $C^{w^*}_{m,3/4}$ in Fig. 10(a), it can be seen from Fig. 10(b) that the cell potential drops to zero for $C^{w^*}_{m,3/4} \leq 1.0$, with no reversals observed for further increase in the water uptake. It is also noted from Fig. 10(b) that for there exists no voltage reversals for $C^{w^*}_{m,1/4}$ and $C^{w^*}_{m,3/4} \geq 1.1$, implying no considerable improvement in the dynamic behavior for improvements in $C^{w^*}_m$ beyond 1/4th of the membrane thickness.

From Fig. 10 it can be seen that there exists a minimum $C^{w^*}_m$, $(C^{w^*}_{m,b})_{\min}$, for a given $C^{w^*}_{m,0}$ and thickness in the membrane, such that the voltage reversal can be avoided. The variation of $(C^{w^*}_{m,b})_{\min}$ with the membrane overhydration fraction, b/L (see inset in Fig. 11), for $C^{w^*}_{m,0} = 0.7,\ 0.8,\ 0.9$ and 1.0, is presented in Fig. 11. It can be seen that there exists a considerable difference in the amount of overhydration required to avoid voltage reversal for $b/L = 0.25$, for the different values of $C^{w^*}_{m,0}$. The cell voltage drops to zero for $C^{w^*}_{m,b} < 1.20,\ 1.15,\ 1.10$ and 1.075 for $C^{w^*}_{m,0} = 0.7,\ 0.8,\ 0.9$ and 1.0, respectively, as seen from the values of $(C^{w^*}_{m,b})_{\min}$. It is noted that the $(C^{w^*}_{m,b})_{\min}$ decreases monotonously with the increase in overhydration fraction, with no significant difference in the values of $(C^{w^*}_{m,b})_{\min}$ for $b/L > 0.50$. This behavior can be attributed to the effects of electro-osmotic drag being significantly dominant at near the anode region, and the improvements in the back diffusion rate with increase in $C^{w^*}_m$ along the length of the membrane. It is also noted that with the increase in $C^{w^*}_{m,0}$, the difference in the $(C^{w^*}_{m,b})_{\min}$ drops significantly along the length of the membrane, as seen in Fig. 11.

The results presented in this section offer insight into the effects of various membrane properties on the hydration of the membrane during transient operation of fuel cells. Future work could include a study of various existing membranes, such as reinforced membranes, hydrocarbon membranes and others, using the present model. The effects of load change on mechanical behavior of membrane are also significant, as presented in Ref. [23] and could also be investigated for cases leading to anode dryout. The model can also be used to study the dry startup behavior of PEM fuel cells and to optimize operating parameters to improve performance as it closely emulates the actual load changes for automotive applications. Also, other factors such as reactant starvation during startups and load changes can lead to reversal in voltage and cause irreversible damage to the MEA [24] and can be studied in future. The combinations of water uptake explored in the present study serve as a proof of concept of a graded membrane design, and can be further optimized in a future work to suit desired performance characteristics. A more detailed study would be to solve an optimization problem to determine the optimized variation in uptake capacity for given load capacity or performance characteristics. By averting voltage reversals, the graded design of membrane also improves the operating range of the fuel cell to large current densities.

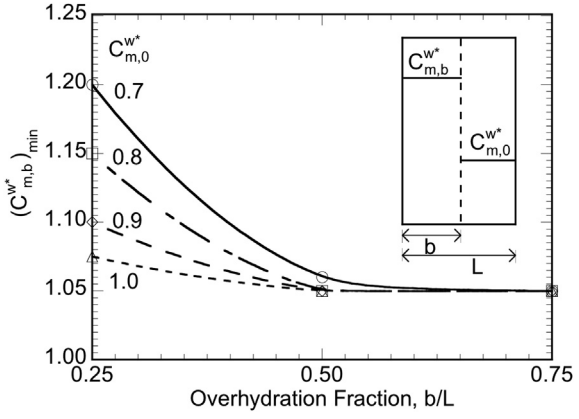

Fig. 11. Variation in $(C^{w^*}_{m,b})_{\min}$ as a function of membrane overhydration fraction, b/L, for various $C^{w^*}_{m,0}$.

4. Conclusions

A comprehensive analysis of the effects of membrane properties on the cell voltage response of a single-channel PEM fuel cell was presented, based on the numerical simulations for low humidity operations. It was shown that a sudden increase in current density can lead to anode dryout, causing voltage reversal and may lead to cell degradation. The voltage response was shown to be strongly correlated to the membrane properties and also the water diffusion in porous media. It was also shown that the voltage reversals can be averted by employing graded membrane approach. The results provide insight in designing and choosing membranes for particular applications.

Nomenclature

A	superficial electrode area [m^2]
C_k	molar concentration of species k [mol m^{-3}]
D	mass diffusivity of species [m^2 s^{-1}]
E_{cell}	cell potential or voltage [V]
EW	equivalent weight of dry membrane [kg mol^{-1}]
F	Faraday constant [96,487 C $equivalent^{-1}$]
j	transfer current [A m^{-3}]
K	permeability [m^2]
n_d	electro-osmotic drag coefficient [H_2O/H^+]
p	pressure [bar]
R	universal gas constant [8.314 J mol^{-1} K^{-1}]
RH	relative humidity
S	source term in transport equations
T	temperature [K]
$\vec{u}$	velocity vector

Greek letters

α	transfer coefficient
ε	porosity
η	surface overpotential [V]
λ	membrane water content
μ	viscosity [kg m^{-1} s^{-1}]
ρ	density [kg m^{-3}]
σ	electronic conductivity [S m^{-1}], ionic conductivity [S m^{-1}]
τ	shear stress [N m^{-2}]; tortuosity
ϕ	phase potential [V]

Superscripts and subscripts

a	anode
c	cathode
cell	single fuel cell
e	electrolyte
eff	effective value
eq	equivalent
g	gas phase
in	inlet
k	species
m	membrane phase
0	$t = 0$ s, initial state
ref	reference value
s	electronic phase
sat	saturated value
SS	steady state
t	time > 0 s
w	water

References

[1] C.Y. Wang, Chem. Rev. 104 (2004) 4727–4766.
[2] M.L. Perry, T.F. Fuller, J. Electrochem. Soc. 149 (7) (2002) S59–S67.
[3] J. Hamelin, K. Agbossou, A. Laperriere, F. Laurencelle, T.K. Bose, Int. J. Hydrogen Energy 26 (6) (2001) 625–629.
[4] S. Kim, S. Shimpalee, J.W. Van Zee, J. Power Sources 135 (1/2) (2004) 110–121.
[5] S. Kim, S. Shimpalee, J.W. Van Zee, J. Power Sources 137 (1) (2004) 43–52.
[6] J. Benziger, E. Chia, J.F. Moxley, I.G. Kevrekidis, Chem. Eng. Sci. 60 (2005) 1743–1759.
[7] Q. Yan, H. Toghiani, H. Causey, J. Power Sources 161 (1) (2006) 492–502.
[8] S. Um, C.Y. Wang, K.S. Chen, J. Electrochem. Soc. 147 (12) (2000) 4485–4493.
[9] J.C. Amphlett, R.F. Mann, B.A. Peppley, P.R. Roberge, A. Rodrigues, J. Power Sources 61 (1–2) (1996) 183–188.
[10] P.R. Pathapati, X. Xue, J. Tang, Renewable Energy 30 (2005) 1–22.
[11] X. Xue, J. Tang, A. Smirnova, R. England, N. Sammes, J. Power Sources 133 (2) (2004) 188–204.
[12] M. Ceraolo, M. Miulli, A. Pozio, J. Power Sources 113 (1) (2003) 183–188.
[13] Y. Wang, C.Y. Wang, Electrochim. Acta 50 (2005) 1307–1315.
[14] Y. Wang, C.Y. Wang, Electrochim. Acta 51 (2005) 3924–3933.
[15] P.W. Majsztrik, Mechanical and Transport Properties of Nafion for PEM Fuel Cells; Temperature and Hydration Effects (Ph.D. thesis), in Chemistry, Princeton University, Princeton, NJ, 2008.
[16] T.A. Zawodzinski, T.E. Springer, F. Uribe, S. Gottesfeld, Solid State Ionics 60 (1993) 199–221.
[17] S. Slade, S.A. Campbell, T.R. Ralph, F.C. Walsh, J. Electrochem. Soc. 149 (12) (2002) A1556–A1564.
[18] T.A. Zawodzinski, C. Derouin, S. Radzinski, R. Sherman, V.T. Smith, T.E. Springer, S. Gottesfeld, J. Electrochem. Soc. 140 (12) (1993) 1041–1047.
[19] Y. Zhang, A. Mawardi, R. Pitchumani, ASME J. Fuel Cell Sci. Technol. 3 (4) (2006) 464–476.
[20] R.B. Bird, W.E. Stewart, E.N. Lightfoot, Transport Phenomena, Wiley, New York, 1960.
[21] T.E. Springer, T.A. Zawodzinski, S. Gottesfeld, J. Electrochem. Soc. 138 (8) (1991) 2334–2342.
[22] S. Motupally, A.J. Becker, J.W. Weidner, J. Electrochem. Soc. 147 (9) (2000) 3171–3177.
[23] A. Verma, R. Pitchumani, ASME J. Fuel Cell Sci. Technol. 11 (3) (2014) 031009, http://dx.doi.org/10.1115/1.4026551, 9pp.
[24] A. Taniguchi, T. Akita, K. Yasuda, Y. Miyazaki, J. Power Sources 130 (2004) 42–49.
[25] ANSYS® Academic Research, Release 14.0, Help System, Fluent® Theory Reference, ANSYS, Inc.